

Tubular precipitation and redox gradients on a bubbling template

David A. Stone* and Raymond E. Goldstein†‡§

*Department of Soil, Water, and Environmental Science, †Department of Physics, and ‡Program in Applied Mathematics, University of Arizona, Tucson, AZ 85721

Communicated by Herman Z. Cummins, City College of the City University of New York, New York, NY, June 25, 2004 (received for review May 6, 2004)

Tubular structures created by precipitation abound in nature, from chimneys at hydrothermal vents to soda straws in caves. Their formation is controlled by chemical gradients within which precipitation occurs, defining a surface that templates the growing structure. We report a self-organized periodic templating mechanism producing tubular structures electrochemically in iron-ammonium-sulfate solutions; iron oxides precipitate on the surface of bubbles that linger at the tube rim and then detach, leaving behind a ring of material. The acid-base and redox gradients spontaneously generated by diffusion of ammonia from the bubble into solution organize radial compositional layering within the tube wall, a mechanism studied on a larger scale by complex Liesegang patterns of iron oxides formed as ammonia diffuses through a gel containing FeSO₄. When magnetite forms within the wall, a tube may grow curved in an external magnetic field. Connections with free-boundary problems in speleothem formation are emphasized.

Templating processes that produce tubular structures span an enormous range of scales and mechanisms. At one extreme are iron-sulfide chimneys 30 m high over hydrothermal vents (1), formed by precipitation at the interface between upwelling, acidic, hot, mineral-rich fluid and colder, alkaline surrounding seawater. There is fossil evidence of millimeter-scale hollow “botryoidal” (grape-like) clusters and chimneys of iron sulfide at seafloor hydrothermal seepages (2). Tubular fossilized “algal structures,” possibly biogenic, are found in sedimentary layers of banded iron formations (3). Biogenic examples include mollusk shells, which form, in part, because of chemical gradients maintained by pumping mechanisms in the mantle (4), and certain bacteria, the anionic polysaccharide sheath of which attracts and bonds metal cations, which can produce tubular structures templated by the organism’s cell body (5). Recent work has also determined that polysaccharide strands extruded from microorganisms can act as templates for iron oxyhydroxide precipitation (6), and filaments of bacterial cells can even be used as templates for synthetic mineralization (7). Speleothem formation in limestone caves provides another pertinent example. As water flows down a structure and lingers as a pendant drop, dissolved carbon dioxide outgasses, raising the pH, and supersaturated calcium carbonate precipitates on the drop. Detachment of the drop leaves a thin ring of material attached to the growing tube; repetition of this process produces straight “soda straws” or curved “helictites” (8). Precipitative film formation on bubbles has also been demonstrated in electrodeposition (9). Finally, tree-like “silicate gardens” (10–12) grow in sodium silicate solutions seeded with metal ion salts, possibly from osmotic stresses across a silicate gel membrane, and now can be studied in a very controlled manner (13).

We describe here a self-organized process by which tubular structures grow from the templating action of gas bubbles (Fig. 1). Produced at the cathode of an electrochemical cell, these bubbles support a precipitative film formed at the gas–solution interface; detachment of the bubble leaves a ring of material that extends the tube, and the process continues. Mechanistically, this is a phase-reversed version of soda-straw growth in caves. With bubbles detaching at intervals of one to several seconds, these

“ferrotubes” grow to millimeters in tens or hundreds of minutes, orders of magnitude faster than their geological counterparts, and thus may serve as a model system for the study of tubular growth. Our studies highlight a class of important yet previously little-studied free-boundary problems in precipitative pattern formation. The chemical building blocks of these structures are simple, and if present in a well mixed system, the resulting mass precipitation has little geometric structure. Only through the templating action of bubbles and the redox gradient does the regular tubular geometry emerge. In addition, we find a second level of structure: the iron oxides/hydroxides in the tube wall are arranged in an oxidation sequence. Although a quantitative theory of tube growth does not exist yet, our observations establish key processes that must be considered.

Templating Chemistry

Structures similar to ferrotubes have been reported anecdotally in studies of the aqueous corrosion of iron as whiskers (14), “corrosion tubes” (15), or “chimneys” (16). Observations of bubbles emerging from the tube openings led to the suggestion that this gas was hydrogen and its venting acts to keep tubes open (16). As is typical, in our experiment reductive hydrolysis of water [$2\text{H}_2\text{O} + 2\text{e}^- \rightarrow \text{H}_2(\text{g}) + 2\text{OH}^-$] takes place at the cathode, so the bubbles are primarily hydrogen gas. The electrochemical protocol is simple; the electrolyte is an aqueous mixture of Fe(II)(NH₄)₂(SO₄)₂·7H₂O and Fe(III)(NH₄)₂(SO₄)₂·12H₂O in the ratio of 6:1 to 12:1, with a total iron molarity ranging from 0.6 to 0.9 M. The cathode and anode are typically mild steel and spaced ≈8 cm apart. Tubes are grown at constant current, with average current densities of 80–120 mA/cm² based on the bare surface area of the cathode and dc voltages ranging from 2 to 4 V. Across the surface of the cathode the current density is naturally inhomogeneous, giving rise to isolated streams of bubbles, gradients of different iron-oxide species (including metallic iron), and tube growth at particular sites. Microelectrodes and pH indicators show that the starting solution is highly acidic (pH ≤ 2.5) far from the cathode but basic (pH ≥ 10) within a thin boundary layer around it. Although the bulk solution continually oxidizes because of the effects of the anode, the precipitation of oxidized iron actually occurs at the cathode, where hydroxide ions are produced. Nominally pure ferrous ammonium-sulfate solutions only produce tubes after current has flowed for many hours, during which the solution slowly oxidizes, raising the ferric/ferrous ratio, $r = [\text{Fe(III)}]/[\text{Fe(II)}]$. We found that tubes would begin growing within 20 min if the initial value of r was ≈0.08–0.16.

The precipitate film forms over the bubble surface within seconds of its emergence from the tube. As the bubble grows, the film fractures into polygonal sections that are advected around the surface by the fluid flow; most sections are lost when the

Abbreviations: GR2, green rust; Eh, redox potential.

§To whom correspondence should be addressed at: Department of Physics, University of Arizona, 1118 East 4th Street, Tucson, AZ 85721. E-mail: gold@physics.arizona.edu.

© 2004 by The National Academy of Sciences of the USA



Fig. 1. Ferrotubes growing in solution. (Scale bar, 5 mm.)

bubble detaches. Material at the contact line (at which tube, bubble, and solution meet) remains to form an irregular ring around the rim, adding to the growth of a freestanding tube. Addition of acid to the solution slowly dissolves the tubes, rendering them transparent just before they break apart. We observed that bubbles rise up from deep inside the tube, near its base, and are not simply formed at its open end.

Attempts to produce tubes without current were conducted by introducing a stream of hydrogen gas bubbles into the solution. Only in the additional presence of gaseous NH_3 would precipitation occur. Also, if aqua ammonia is injected into the acidic electrolyte, columnar precipitates immediately form (Fig. 2A), although they lack cohesiveness. These columns are very similar to silicate gardens (10, 11). The well established reaction pathways by which ammonia can precipitate white rust $[\text{Fe}(\text{II})(\text{OH})_2]$ or green rust (GR2) $[\text{Fe}(\text{II})_4\text{Fe}(\text{III})_2(\text{OH})_{12}\text{SO}_4 \cdot n\text{H}_2\text{O}]$ (17) and the striking blue-green color of the tubes suggest that they, as well as the film precipitating on the templating bubbles, are indeed GR2. Both GR2 and white rust are unstable, and can readily oxidize partially to magnetite $[\text{Fe}(\text{II})\text{Fe}(\text{III})_2\text{O}_4]$ or fully to lepidocrocite $[\gamma\text{-Fe}(\text{III})\text{OOH}]$ (18, 19). This oxidation is driven by the progressive oxidation of the solution from the anodic reaction $2\text{H}_2\text{O} \rightarrow 4\text{H}^+ + \text{O}_2 + 4\text{e}^-$.

Materials Analysis

How is the oxidation sequence described arranged within the tube wall? As is known in corrosion science and geochemistry, typical environmental conditions found on exposed steel or in wet soils straddle the major ferrous–ferric division among the iron oxides/hydroxides/oxyhydroxides. For example, hollow corrosion “tubercles” or “blisters” forming on ferrous metals typically exhibit a tripartite stratification with oxidized species such as lepidocrocite on the outside, reduced species such as GR2 on the inside, and magnetite sandwiched between (16, 20, 21). Materials analysis confirms precisely this spatial organization in the tubes. Mössbauer spectroscopy indicated a complex mix of ferrous and ferric species along with some completely reduced metallic iron (Fe^0); transmission electron microscopy/energy-dispersive x-ray analysis and x-ray diffraction positively identified lepidocrocite and magnetite. Scanning electron microscopy images clearly reveal three distinct layers (Fig. 3A). The hexagonal plates on the inside of the tube shown in Fig. 3B are characteristic of GR2 (22, 23) or an oxidized allomorph of it such as goethite ($\alpha\text{-FeOOH}$). The interconversion of GR2 to magnetite is seen in Fig. 3C as magnetite nodules forming on the plates. Finally, Fig. 3D shows the characteristic lath-like lepidocrocite crystals along with octahedral magnetite crystals.

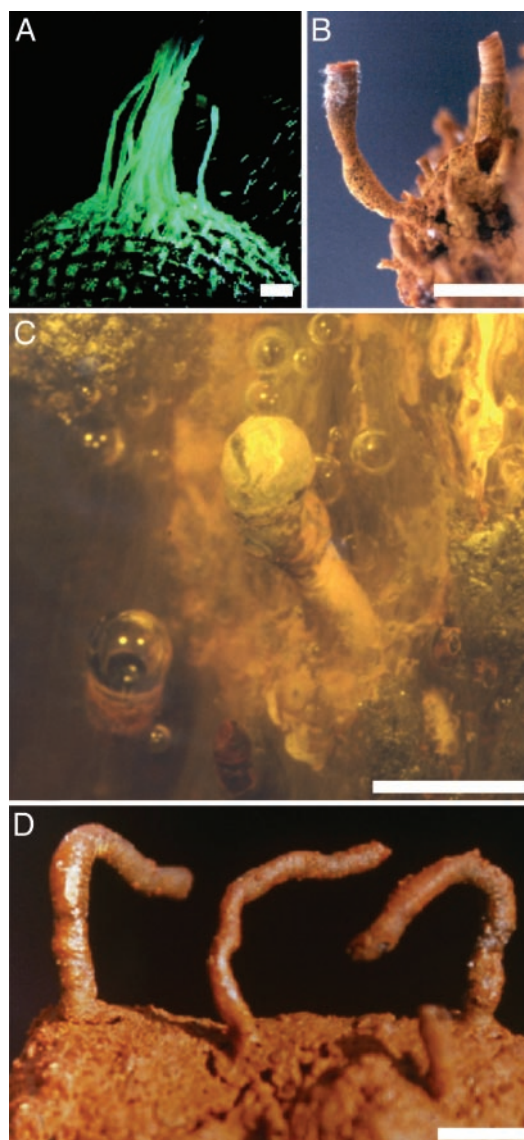


Fig. 2. Tube morphologies. (A) Columnar precipitation around injected jets of aqua ammonia. (B) Tube diameter varying as current is transiently decreased (narrow region) then increased and held at a higher level (wider upper half of tube). (C) Encapsulated (botryoidal) morphology. (D) Bent tubes grown over small magnets. (Scale bars, 5 mm.)

Templating Physics

Under typical experimental conditions, the hang time τ of a bubble of radius $R \approx 1$ mm on the end of a tube is ≈ 1 s, giving a mean volumetric flow rate $Q = 4\pi R^3/3\tau \approx 4 \times 10^{-3} \text{ cm}^3/\text{s}$. Using the bare air–water surface tension σ , we find a negligible capillary number $Ca = \eta Q/a^2\sigma \approx 4 \times 10^{-5}$, and thus the bubble growth rate can be considered quasistatic. Because the diffusion constant of ammonia in the gas phase is $D_g \approx 10^{-2} \text{ cm}^2/\text{s}$, τ is comparable to the time $\tau_g \approx R^2/D_g \approx 1$ s for ammonia to diffuse across the bubble, which is thus equilibrated with respect to ammonia. However, the very much smaller diffusivity of dissolved ammonia in solution, $D_s \approx 10^{-5} \text{ cm}^2/\text{s}$, implies that only a region on the order of $\sqrt{D_s\tau} \approx 30 \mu\text{m}$ within the fluid participates in the precipitation, providing an estimate of the film thickness. Indeed, the classic Smoluchowski flux $Q_s = 4\pi RC_\infty D$ associated with the equilibrium concentration profile $C(r) = C_\infty(1 - R/r)$, where C_∞ is the asymptotic concentration, would be inapplicable here, because the time to attain the equilibrium

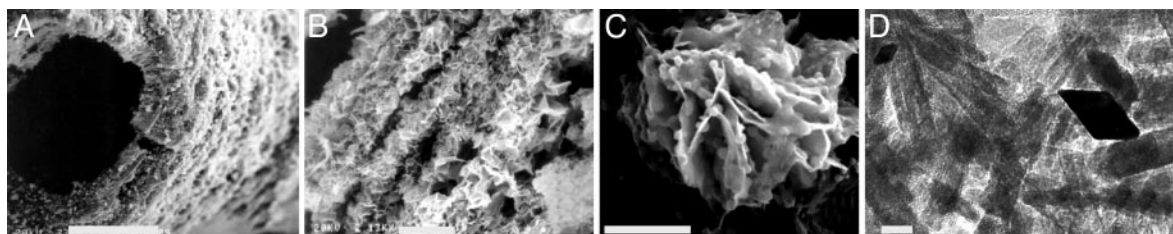


Fig. 3. Ferrotube microstructure. Scanning electron microscope images of tube, showing tripartite layering (A) (scale bar, 100 μm), GR2 crystals on the inside wall of tube (B) (scale bar, 10 μm), and GR2 crystals and magnetite nodules (C) (scale bar, 5 μm) and transmission electron microscope image of lepidocrocite laths and magnetite crystals (D) (scale bar, 10 nm).

profile would be $\tau_s \approx R^2/D_s \approx 100 \text{ s} \gg \tau$. Often, a forest of tubes grows off an extended cathode that produces bubbles across its entirety, and a detailed model of the growth of the thin precipitative film then requires consideration of the large fluid flow entrained by the great number of rising bubbles. We estimate a typical fluid velocity $U \approx 1 \text{ cm/s}$. With $\nu = 0.01 \text{ cm}^2/\text{s}$ the kinematic viscosity of water, the Reynolds number $Re = UR/\nu \approx 10$, implying laminar flow, but the Peclet number $Pe = UR/D_s \approx 10^4$, and thus advection dominates diffusion. This can modify significantly the rate of transport to an absorbing surface (24) and modify the hang time (25). Similar considerations apply to surfactant adsorption onto the surface of growing bubbles (26). The tube radius decreases with decreasing current (Fig. 2B), so at very low currents, when the hang time grows to hundreds of seconds, tubes seal off because the precipitative film is so thick it can withstand the pressure of the bubble. Botryoidal morphologies then can form (Fig. 2C) akin to those in iron-sulfide systems.

A most striking phenomenon is the effect of magnetic fields on growing tubes (Fig. 2D). When small magnets with a surface field on the order of 0.3 T are embedded in the cathode, the tubes sometimes grow with curved shapes. The curving of the tube axis may reflect alignment by the field of the microscopic domains shown in Fig. 3. Although the field axis at the surface of the magnets is parallel to the electrical current, the strongly curved fringing fields of the small magnets bend toward the horizontal some distance above them and will produce a Lorentz force on the ionic current and fluid circulation with a vertical vorticity vector. The helical paths taken by bubbles rising above a magnet on the cathode show this clearly. This flow can create (27, 28) a hydrodynamic boundary layer and mixing in the depletion layer, thereby increasing the limiting current that can flow. Such effects are likely to be important in understanding the morphology shown in Fig. 2D, because these mixing effects vary around the perimeter of the tube.

The spectrum of observations discussed above leads to the model for the growth of ferrotubes shown in Fig. 4. The initial establishment of a growth site involves processes that are complex, even chaotic, and are not discussed here. Five fundamental subsequent stages are proposed, starting at the base of the tube and moving up. (i) Water and H^+ are reduced at the surface of the cathode, producing hydroxide ions and hydrogen gas, and ammonium ions are deprotonated to produce ammonia gas. (ii) The mixed gases move up through the tube as individual bubbles and act as mechanical pumps, pushing the very basic solution up and out of the open top. (iii) When bubbles linger at the tube opening, the basic solution and ammonia react with the bulk, acidic, ferrous solution. GR2 precipitates around the rim and over the surface of the bubble as a thin film. (iv) The bubble detaches, leaving a ring of deposited material around the rim. (v) The GR2 quickly transforms to magnetite within the tube and oxidizes to lepidocrocite on the outside.

Gel Systems

Confronted with the complex diffusion, advection, and precipitation found in the tube-growth environment, it is natural to seek a simplified system that preserves the essential physics: the acid–base and redox gradients. As in controlled studies of Turing patterns in reaction–diffusion systems (29), we found that carrying out the precipitation in a gel affords the necessary simplification. A traveling oxidation–reduction and acid–base gradient is readily established within a ferrous sulfate solution (typically 0.5 M) in 1% agar gel by diffusion of concentrated (17 M) aqua ammonia from a reservoir at one end. Various iron hydr(oxides) stratify along this gradient, and their appearance can be effectively depicted on a Pourbaix diagram, commonly used in geochemistry to define stability relations among components of a system at thermodynamic equilibrium in terms of the proton-motive force (quantified through the pH) and the redox potential [Eh = $(RT/F)\ln a_e$, where a_e is the electron activity, R is the gas constant, T is the absolute temperature, and F is the Faraday constant]. The numerous, complex interrelationships between all the components of the system, with their various effects on redox potentials (causing Eh changes) and participation in (de)protonation reactions (causing pH changes), are summarized on this diagram, in which every line represents an equilibrium between two species. By expanding the Eh/pH gradient over macroscopic scales and following the sequential precipitation in time, we not only create an expanded version of the tube wall (and of the other stratified systems described

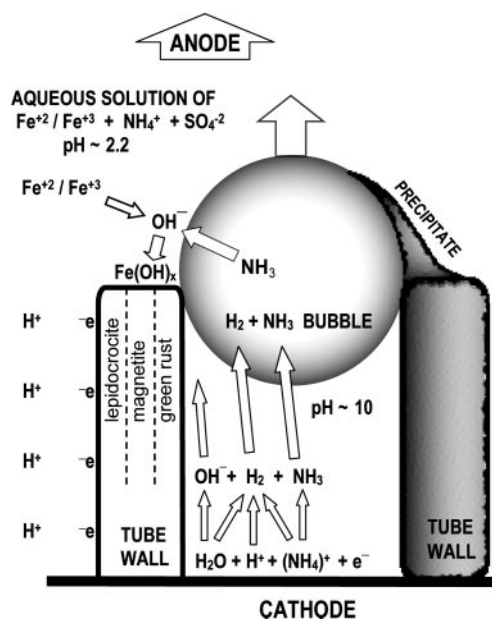


Fig. 4. Mechanisms involved in tubular precipitation templated by bubbles.

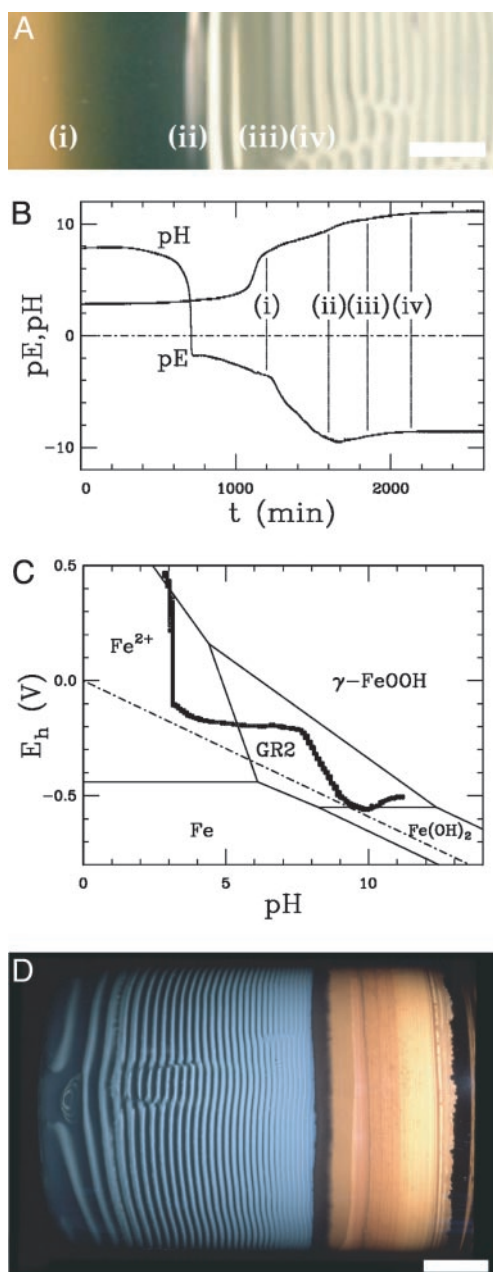


Fig. 5. Liesegang band formation. (A) Bands formed as ammonia diffused from right to left. (Scale bar, 5 mm.) Transition points i–iv correspond to pH and pE [$-\log(\text{electron activity})$] traces shown in B, plotted together in C on a Pourbaix diagram, following Génin *et al.* (30–32). The dashed line in C indicates the stability limit of water. (D) Liesegang band pattern formed by diffusion of ammonia and subsequent oxidation, leaving a pattern characterized by a gradient in oxidation from left to right. (Scale bar, 1 cm.)

above) but also a spatiotemporal realization of the Pourbaix diagram by instrumenting the gel with appropriate electrodes (Microelectrodes, Bedford, NH). In our case, these electrodes give a spatial resolution set by the width of the probes (1 mm) and a temporal resolution of ≈ 30 s.

This experimental setup is used to study Liesegang ring formation (33), and as shown in Fig. 5A, the diffusing ammonia front may leave behind bands and gaps that show the classical linear increase in width and spacing with band number. Strangely, and unlike any other known Liesegang system (34), within millimeters the pattern disappears into a dark, obscuring

layer only to reemerge after a few more millimeters, although with the contrast reversed: the white bands are now dark and the gaps are now filled in with a light-gray precipitate. The temporal behavior of the Eh and pH measured 3.0 cm below the aqua ammonia reservoir is shown in Fig. 5B. For the purposes of representation on the same scale as pH, it is often convenient to define $pE = -\log a_e$; thus, if Eh is measured in volts, then $pE = 16.9 \text{ Eh}$. The pH begins at ≈ 3 , reflecting the acidifying character of the ferrous sulfate solution and eventually rises to ≈ 11 , far behind the front, but its temporal derivative decreases above pH 7 as hydroxyl ions incorporate into iron hydroxides. The Eh, by contrast, displays a much earlier, steep drop (up to 500 mV in minutes, whereas the pH hardly changes) followed by a slow decline. When superimposed on the Pourbaix diagram (30–32) in Fig. 5C, we see that the system moves from the region of ferrous ion stability through the GR2 zone into the white-rust domain and then back into the GR2 zone, tracking the appearance of a white-rust band and then the obscuring zone and finally the gray precipitate. The trajectory also approaches the stability boundary of water at $pH \approx 3$ and touches it at $pH \approx 9$, which is consistent with the observation of occasional spontaneous production of gas bubbles (hydrogen) in the gel both before and after precipitation bands form.

Although the mechanisms of diffusion, precipitation, and depletion that underlie Liesegang ring formation are well understood, controversy remains regarding the growth dynamics (e.g., nucleation vs. Ostwald ripening). In our system, we observe by light microscopy under high magnification that the initial white bands are composed of spindle-shaped crystallites, which soon dissolve as a second spheroidal phase emerges to produce the contrast-reversed bands. This remarkably complex banding also depends very sensitively on the ferrous/ferric ratio. No theoretical model yet explains these observations. The proposal that stratified oxidation states of iron in the gel system represent an expansion of the tube wall is made complete by allowing oxygen to diffuse into a Liesegang system after the ammonia, just as the bulk solution oxidizes the external surface of growing tubes. This process leads to a tripartite structure of the gel precipitates (Fig. 5D, with orange lepidocrocite, black magnetite, and GR2), just as in the tube wall.

Reversed-Phase Experiments

The template has the dual roles of a support for a precipitative film and the locus of a redox gradient. This template could have

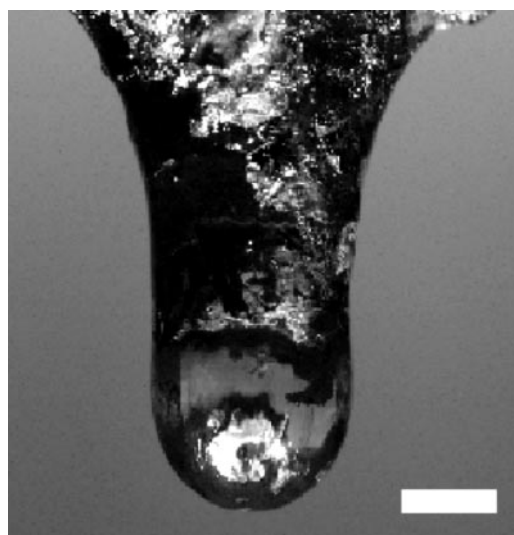


Fig. 6. Reversed-phase growth of an iron-sulfide tube. (Scale bar, 2 mm.)

almost any geometry: convex, concave, planar, or columnar. The growth mechanism of soda-straw speleothems mentioned above suggests the obvious possibility of a phase-reversed version of the ferrotube system. We achieved this by pumping a 0.5 M solution of ferrous sulfate through a small tube into a chamber filled with gaseous ammonia or hydrogen sulfide, expecting that diffusion into the solution would cause a precipitative film to form on the pendant drop, followed by the usual processes of detachment and reprecipitation. Fig. 6 confirms that this arrangement indeed produces a hanging tube growing downward as successive drops detach and leave a ring of material. Using ammonia, the tubes are composed of magnetite, and using H₂S, the tubes are composed of ferrous sulfide. The growth rate can be quite fast: 3 cm/hour with a diameter of 4 mm.

Conclusions

Tube generation by bubble templating suggests possible applications in the formation of microtubes with interesting chemical, magnetic, and mechanical properties. One avenue of interest involves the formation of suitable polymeric composites to

decrease the inherent brittleness of ferrotubes. The clear correspondence to geophysical phenomena involving precipitative pattern formation, particularly hydrothermal vents, leads naturally to more speculative avenues for future study. Two clear directions include anoxic sulfidic chemistry and calcareous speleothem growth. Russell and coworkers (35–37) hypothesized about the possible role structures such as those in Figs. 1 and 2 may have played in the attraction, synthesis, and concentration of polyanionic organic molecules as a first step toward the emergence of life. The strong redox gradients and the encapsulation possible as ferrotubes form suggest their possible role in the study of prebiotic synthesis of the molecules of life.

We thank the late Arthur Winfree for inspiring this work; J. C. Baygents, J. W. Beck, K. Callerame, J. Curry, and C. Jarvis for important discussions and ongoing collaborations; and S. Seraphim, D. Agresti, and P. Anderson for assistance with the materials characterization. This work was supported by the vice president for research and the dean of science at the University of Arizona, the Research Corporation, and the National Science Foundation Information Technology Research program (Grant PHY-0219411).

1. Corliss, J. B., Dymond J., Gordon, L. I., Edmond, J. M., Herzen, R. P. V., Ballard, R. D., Green, K., Williams, D., Bainbridge, A., Crane, K. & van Andel, T. H. (1979) *Science* **203**, 1073–1083.
2. Boyce, A. J., Coleman, M. L. & Russell, M. J. (1983) *Nature* **306**, 545–550.
3. Barghoorn, E. S. & Tyler, S. A. (1965) *Science* **147**, 563–577.
4. Bonucci, E. (1992) in *Calcification in Biological Systems* (CRC, Boca Raton, FL), p. 179.
5. Provencio, P. P. & Polyak, V. J. (2001) *Geomicrobiol. J.* **18**, 297–309.
6. Chan, C. S., De Stasio, G., Welch, S. A., Girasole, M., Frazer, B. H., Nesterova, M. V., Fakra, S. & Banfield, J. F. (2004) *Science* **303**, 1656–1658.
7. Davis, S. A., Burkett, S. L., Mendelson, N. H. & Mann, S. (1997) *Nature* **385**, 420–423.
8. Hill, C. & Forti, P. (1997) *Cave Minerals of the World* (Natl. Speleological Soc., Huntsville, AL).
9. Tsai, W. L., Hsu, P. C., Hwu, Y., Chen, C. H., Chang, L. W., Je, H. H., Line, H. M., Groso, A. & Margaritondo, G. (2002) *Nature* **417**, 139.
10. Cartwright, J. H. E., Garcia-Ruiz, J. M., Novella, M. L. & Otalora, F. (2002) *J. Colloid Interface Sci.* **256**, 351–359.
11. Thouvenel-Romans, S. & Steinbock, O. (2003) *J. Am. Chem. Soc.* **125**, 4338–4341.
12. Coatman, R. D., Thomas, N. L. & Double, D. D. (1980) *J. Mater. Sci.* **15**, 2017–2026.
13. Thouvenel-Romans, S., van Saarloos, W. & Steinbock, O. (2004) *Europhys. Lett.* **67**, 42–48.
14. Butler, G. & Ison, H. C. K. (1958) *Nature* **182**, 1229–1230.
15. Riggs, O. L., Jr., Sudbury, J. D. & Mutchison, M. (1960) *Corrosion* **16**, 94–98.
16. Smith, D. C. & McEnaney, B. (1979) *Corrosion Sci.* **19**, 379–394.
17. Lin, H., Sakamoto, H., Seo, W. S., Kuwabara, K. & Koumoto, K. (1998) *J. Cryst. Growth* **192**, 250–256.
18. Vogel, A. & Svehla, G. (1996) *Vogel's Qualitative Inorganic Analysis* (Longman, Harlow, England), 7th Ed.
19. Cornell, R. & Schwertmann, U. (2003) *The Iron Oxides: Structure, Properties, Reactions, Occurrence and Uses* (VCH, Weinheim, Germany).
20. Bigham, J. M. & Touvinen O. H. (1985) in *Planetary Ecology*, eds. Caldwell, D. E., Brierley, J. A. & Brierley, C. L. (Van Nostrand Reinhold, New York), pp. 239–249.
21. Raman, A., Nasrazadani, S. & Sharma, L. (1989) *Metallography* **22**, 79–96.
22. Bernal, J., Dasgupta, D. & Mackay, A. (1959) *Clay Miner. Bull.* **4**, 15–30.
23. McGill, I. R., McEnaney, B. & Smith, D. C. (1976) *Nature* **259**, 200–201.
24. Acrivos, A. & Taylor, T. D. (1962) *Phys. Fluids* **5**, 387–394.
25. Oguz, H. N. & Prosperetti, A. (1993) *J. Fluid Mech.* **257**, 111–145.
26. Wong, H., Rumschitzki, D. & Maldarelli, C. (1999) *J. Fluid Mech.* **379**, 279–302.
27. Aaboubi, O., Chopart, J. P., Douglade, J., Olivier, A., Gabrielli, C. & Tribollet, B. (1990) *J. Electrochem. Soc.* **137**, 1796–1804.
28. Coey, J. M. D. & Hinds, G. (2001) *J. Alloys Compd.* **326**, 238–245.
29. Castets, V., Dulos, E., Boissonade, J. & De Kepper, P. (1990) *Phys. Rev. Lett.* **64**, 2953–2956.
30. Génin, J.-M. R., Olowe, A. A., Refait, P. & Simon, L. (1996) *Corrosion Sci.* **38**, 1751–1762.
31. Refait, P., Bon C., Simon, L., Bourrié, G., Trolard, F., Bessière, J. & Génin, J.-M. R. (1999) *Clay Miner.* **34**, 499–510.
32. Refait, P., Génin, A., Abdelmoula, M. & Génin, J.-M. R. (2003) *Corrosion Sci.* **45**, 659–676.
33. Liesegang, R. (1896) *Naturwiss. Wochenschr.* **11**, 353–362.
34. Henisch, H. (1988) *Crystals in Gels and Liesegang Rings* (Cambridge Univ. Press, Cambridge, U.K.).
35. Russell, M. J. & Hall, A. J. (1997) *J. Geol. Soc. (London)* **154**, 377–402.
36. Russell, M. J. (2003) *Science* **302**, 580–581.
37. Martin, W. & Russell, M. J. (2003) *Philos. Trans. R. Soc. London B* **358**, 59–83.